Biochemistry **1997,** *36,* 12087−12100

Initial Trajectory of Carbon Monoxide after Photodissociation from Myoglobin at Cryogenic Temperatures[†,‡]

Tsu-Yi Teng, Vukica Šrajer, and Keith Moffat*

Department of Biochemistry and Molecular Biology, The University of Chicago, Chicago, Illinois 60637

Received May 15, 1997; Revised Manuscript Received July 17, 1997[⊗]

ABSTRACT: Migration of the CO ligand following photolysis of carbonmonoxy myoglobin (MbCO) in single crystals has been investigated by time-resolved X-ray diffraction at 40K. After short illumination by weak visible light at a photolysis rate of $\sim 1\ s^{-1}$, the photodissociated CO molecule is found about 1 Å from its bound location. After continuous illumination over several hours, the CO molecule migrates to a more distant site in the distal pocket, about 2.5 Å from its bound location. Migration of the ligand under continuous illumination accounts for different locations of the photodissociated CO molecule previously reported in three cryocrystallographic studies [Teng, T.-Y., et al. (1994) *Nat. Struct. Biol. 1,* 701−705; Schlichting, I., et al. (1994) *Nature 371*, 808−812; Hartmann, H., et al. (1996) *Proc. Natl. Acad. Sci. U.S.A. 93*, 7013−7016]. Due to the different photolysis protocols employed in these studies, each reveals a different part of the trajectory of the photodissociated CO molecule. When the different experimental parts of the trajectory at 40 K are pieced together and combined with our nanosecond time-resolved studies at room temperature [Šrajer, V., et al. (1996) *Science 274*, 1726−1729], excellent agreement is obtained with recent theoretical predictions of the CO probability distribution in the ligand pocket [Vitkup, D., et al. (1997) *Nat. Struct. Biol. 4*, 202−208]. The heme relaxation that accompanies ligand photolysis is incomplete, about 30% of that associated with the conversion of MbCO to deoxy-Mb at room temperature, and independent of the duration of illumination. Other tertiary structural changes in the globin are also greatly diminished. The globin structure is therefore very rigid at cryogenic temperatures, and structural relaxation is greatly hindered, consistent with numerous spectroscopic measurements.

Ligand binding kinetics and ligand trajectories in myoglobin (Mb)[1] have been investigated for decades using spectroscopic techniques (Austin et al., 1975; Alben et al., 1982; Powers et al., 1987; Steinbach et al., 1991; Lim et al., 1995a,b), site-specific mutagenesis (Carver et al., 1992; Huang & Boxer, 1994; Lambright et al., 1994; Springer et al.,1994), X-ray crystallography (Kuriyan et al., 1986; Phillips, 1990; Quillin et al., 1993), and molecular dynamics simulations/energy minimization (Case & Karplus, 1979; Sassaroli & Rousseau, 1986; Elber & Karplus, 1990; Straub & Karplus, 1991; Vitkup et al., 1997), at both ambient and cryogenic temperatures. The picture emerging from these extensive studies [reviewed by Olson and Phillips (1996)] is that initial migration of the photodissociated ligand on the picosecond time scale at ambient temperature is to a site defined by residues Leu 29, Phe 43, His 64, Val 68, and Ile 107, as also predicted by molecular dynamics simulations (Sassaroli & Rousseau, 1986) and observed in cryocrystallographic studies (Teng et al., 1994a; Schlichting et al., 1994; Hartmann et al., 1996). Ligand migration on the longer, nanosecond time scale is less well-characterized, although the ligand remains in contact with residues Leu 29 and Val 68 (Olson & Phillips, 1996), in the general vicinity of the low-temperature site. The exact location of the low-temperature site(s), however, is still in doubt. The three cryocrystallographic experiments differ in experimental conditions (temperature, crystal form, and pH) and protocols (cooling and photolysis), and the photodissociated CO molecule has a well-defined but somewhat different position and orientation in each.

We report here time-resolved studies of the ligand trajectory of the photodissociated CO molecule at cryogenic temperatures using the Laue diffraction method, which allows a very short X-ray exposure time (Moffat, 1997) and thus minimizes the extent of CO rebinding during X-ray data collection. We conducted experiments at both 40 and 20 K and employed two photolysis protocols: short illumination as in our earlier experiment (Teng et al., 1994a) and extended illumination as in the experiments of Schlichting et al. (1994) and Hartmann et al. (1996).

The results enable us to visualize the very slow migration of the CO away from the heme and the limited relaxation of the heme and the globin, under continuous illumination at cryogenic temperatures. That is, we begin to visualize the "protein quake" (Ansari et al., 1985) emanating from the heme after rupture of the Fe−CO bond. The results also provide an explanation for the differences among the three earlier, static studies and attribute them to the varied photolysis protocols and to the use of different crystal forms, each containing a slightly different myoglobin structure with a possibly different dynamics (Phillips, 1990).

However, slow ligand migration is not a unique representation of the results. We also propose a two-site model for

---

[†] This work is supported by grants from the W. M. Keck Foundation and the National Institutes of Health (GM-36452 and RR-07707).

[‡] Coordinates and structure amplitudes for carbonmonoxymyoglobin and its photoproduct at 40 K have been deposited in the Brookhaven Protein Data Bank under the accession codes 1AJG (R1AJGSF) and 1AJH (R1AJHSF).

* To whom correspondence should be addressed.

[⊗] Abstract published in *Advance ACS Abstracts*, September 1, 1997.

[1] Abbreviations: Mb, myoglobin; MbCO, carbonmonoxymyoglobin; MbO_2, oxymyoglobin; Mb*, photoproducts of MbCO; NSLS, National Synchrotron Light Source; PDB, Brookhaven Protein Data Bank.

S0006-2960(97)01140-9 CCC: $14.00 © 1997 American Chemical Society

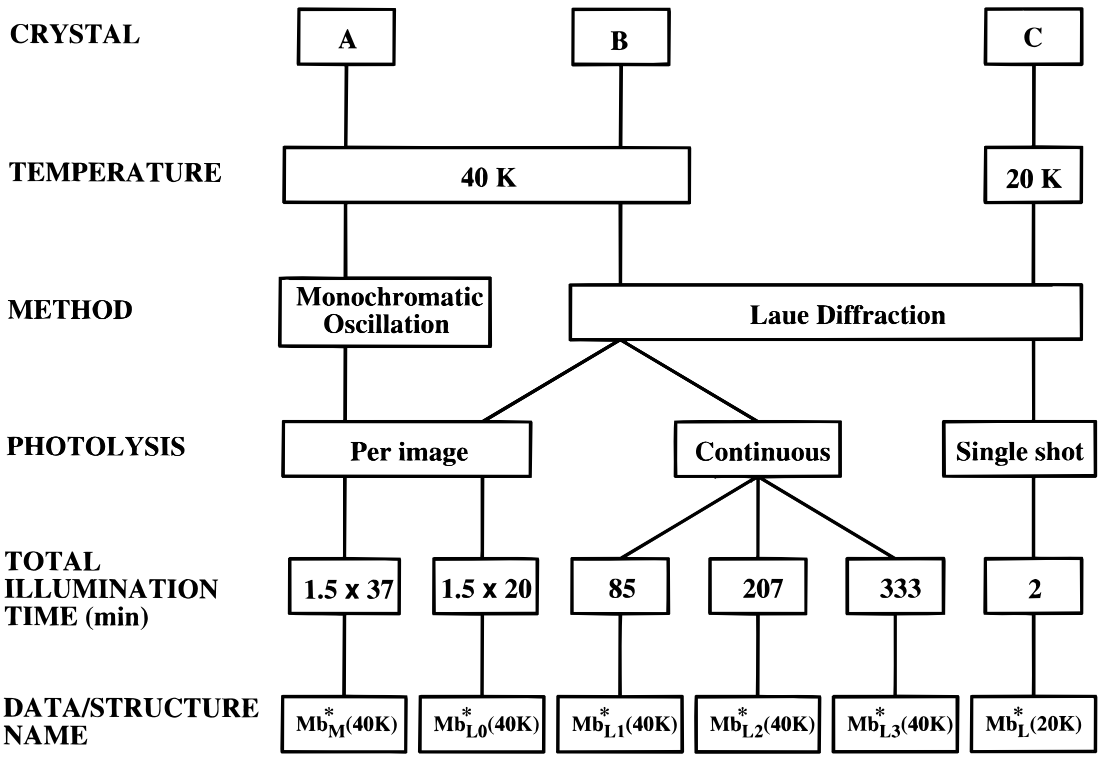

FIGURE 1: Nomenclature of data sets/structures related to key experimental conditions.

the photodissociated CO molecule in the heme pocket upon photolysis of MbCO. In this model, the unbound CO molecule has two possible sites and the population of each site changes with time under continuous illumination.

MATERIALS AND METHODS

Preparation of Crystals, Cooling, Photolysis, and X-ray Data Collection. Details of the preparation of the monoclinic, $P2_1$, form of MbCO crystals at pH 6 and their shock freezing, cryogenic cooling, and monochromatic X-ray data collection at beam line X26C of the NSLS (Brookhaven National Laboratory) are described in Teng et al. (1994a). The MbCO crystals used for X-ray data collection were checked optically for met Mb-content by an on-line single-crystal microspectrophotometer (Chen et al., 1994). Absorption spectra before (MbCO) and after (Mb*) photolysis for the crystals used for data collection were recorded on-line at low temperatures. The spectra are collected using polarized monitoring light, with the light beam perpendicular to the {001} crystal face and the electric vector **E** parallel to the **a** crystal axis. The $P2_1$ crystals are highly dichroic and exhibit a minimum extinction coefficient (and thus a readily measurable optical density) when **E**||**a** (Kendrew & Parrish, 1956). A continuous-working (CW) He-Ne laser at a wavelength of 633 nm was used to photolyze the crystals with a laser power of 1.7 mW and a laser beam size of ~0.2 mm^2.

For the Laue X-ray data[2] at 40 K, the crystal was shock frozen with a cold nitrogen gas stream at 80 K and then cooled to 40 K using a cold helium gas stream (Teng et al., 1994b). The MbCO$_L$(40K) data set was collected, followed by the photoproduct Mb$^*_{L0}$(40K) data set. The photolysis protocol for Mb$^*_{L0}$(40K) was identical to that for Mb$^*_M$(40K) (Teng et al., 1994a): 90 s of laser exposure prior to each frame of X-ray data collection. The crystal was then illuminated continuously by the laser, and Laue data sets Mb$^*_{L1}$(40K), Mb$^*_{L2}$(40K) and Mb$^*_{L3}$(40K) were recorded in sequence. Data set Mb$^*_{L1}$(40K), was therefore collected during the first hour of illumination, Mb$^*_{L2}$(40K) during the third hour, and Mb$^*_{L3}$(40K) during the fifth hour. All Laue data at 40 K were taken on the same crystal with an X-ray exposure time of 8 ms per image, subdivided into two 4 ms segments with an interval of 250 ms between exposures to minimize X-ray heating of the crystal. For the Laue data at 20 K, the MbCO$_L$(20K) Laue data set was recorded first, in a manner similar to that of the MbCO$_L$(40K) data. The crystal was then illuminated once for 120 s by the laser prior to collecting the entire Mb$^*_L$(20K) data set with an X-ray exposure time of 30 ms per image, subdivided into six 5 ms segments. For all Laue data sets, images were recorded at 8° angular intervals through a range of 184°. Figure 1 shows schematically the nomenclature for the present data and structures; Table 1 lists laser illumination, X-ray exposure, and other experimental details for the present data sets and for earlier studies (Teng et al., 1994a; Schlichting et al., 1994; Hartmann et al., 1996).

Data Reduction. All diffraction data were recorded on 250 × 200 mm Fuji HR-III$_N$ image plates and scanned on a 100 μm raster using a Fuji BAS2000 scanner. Both MbCO$_M$(40K) and Mb$^*_M$(40K) monochromatic oscillation data sets, which have 37 images/set, were autoindexed, geometry-refined, and integrated by the program DENZO (Otwinowski, 1991) and scaled by programs in the CCP4 suite (CCP4, 1979). The Laue data, which have 20−28 images/set, were reduced by the program LaueView (Ren & Moffat, 1995a) with energy overlap deconvolution (Ren & Moffat, 1995b). Table 2 gives detailed data reduction statistics. The high

---

[2] X-ray data and structures are labeled with a subscript M to denote monochromatic oscillation [e.g., MbCO$_M$(40K)] or with a subscript L to denote Laue diffraction [e.g., Mb$^*_L$(20K)]. The temperature of the measurement is specified within brackets. Those with subscript L followed by the number 0, 1, 2, or 3 identify different protocols of photolysis/Laue X-ray data collection (see Materials and Methods, Figure 1, and Table 1 for details).

Table 1: Experimental Protocols[a]

	Mb$^*_{\mathrm{L0}}$(40K)	Mb$^*_{\mathrm{L1}}$(40K)	Mb$^*_{\mathrm{L2}}$(40K)	Mb$^*_{\mathrm{L3}}$(40K)	Mb$^*_{\mathrm{M}}$(40K)	Mb$^*_{\mathrm{L}}$(20K)	Mb$^*_{\mathrm{S}}$(20K)	Mb$^*_{\mathrm{H}}$(36K)
crystal								
space group	$P2_1$	$P2_1$	$P2_1$	$P2_1$	$P2_1$	$P2_1$	$P6$	$P2_1$
size (μm^3)	320 × 120 × 50	320 × 120 × 50	320 ×120 × 50	320 × 120 × 50	NR	NR	150 × 150 × 200	300 × 400 × 500
cooling								
cryostat	liquid N$_2$/He open flow	liquid N$_2$/He open flow	liquid N$_2$/He open flow	liquid N$_2$/He open flow	liquid N$_2$/He open flow	liquid N$_2$/He open flow	He gas/liquid stream	liquid He closed cycle
final temperature (K)	40	40	40	40	40	20	20	36
shock freezing protocol	cold N$_2$ gas	cold N$_2$ gas	cold N$_2$ gas	cold N$_2$ gas	cold N$_2$ gas	cold N$_2$ gas	He gas/liquid stream	liquid propane
photolysis								
light source	CW He/Ne laser	CW He/Ne laser	CW He/Ne laser	CW He/Ne laser	CW He/Ne laser	CW He/Ne laser	fiber optic illuminator	laser diode
wavelength (nm)	633	633	633	633	633	633	white light	690
power (mW)	1.7	1.7	1.7	1.7	1.7	1.7	NR	20
focal spot diameter (mm)	0.5	0.5	0.5	0.5	0.5	0.5	NR	1
photolysis protocol	90 s of illumination/ image	continuous; X-ray exposure after 5 min of illumination	continuous; X-ray exposure after 2.7 h of illumination	continuous; X-ray exposure after 4.8 h of illumination	90 s of illumination/ image	single 120 s iilumination	continuous for two data sets	continuous; X-ray exposure after 5 min of illumination
total illumination time (min)	30	85	207	333	56	2.0	132 or 76	120 + 120
photolysis rate (s^{-1})	∼1	∼1	∼1	∼1	∼1	∼1	0.003−0.3	1−10
data acquisition								
method	Laue diffraction	Laue diffraction	Laue diffraction	Laue diffraction	monochromatic oscillation	Laue diffraction	monochromatic oscillation	monochromatic oscillation
experiment time/image	2 × 4 ms	2 × 4 ms	2 × 4 ms	2 × 4 ms	3 min	6 × 5 ms	NR	NR
elapsed time/data set (min)	45	80	45	45	∼180	35	132 or 76	120 + 120
observations	52 218	51 054	56 844	56 893	51 604	28 134	93 946	NR
unique reflections	9 996	10 007	10 145	10 209	13 618	5 632	25 553	11 908
resolution (Å)	1.8	1.8	1.8	1.8	1.7	2.0	1.5	1.7
completeness (%)	79.2	79.8	80.0	80.5	95.8	65.6	77.0	80.1

[a] See the text, Figure 1, and footnote 2 for the definition of data sets in this work; Mb$^*_{\mathrm{S}}$(20K)and Mb$^*_{\mathrm{H}}$(36K) are from Schlichting et al. (1994) and Hartmann et al. (1996), respectively. NR, not recorded.

Table 2: Data Reduction and Refinement

	MbCO$_L$(40K)	Mb$^*_{L0}$(40K)	Mb$^*_{L1}$(40K)	Mb$^*_{L2}$(40K)	Mb$^*_{L3}$(40K)	MbCO$_M$(40K)	Mb$^*_M$(40K)	Mb$^*_L$(20K)
data reduction								
R_{merge} (%)^a	16.3	14.9	17.2	17.7	17.9	4.9	5.0	20.0
R_{MbCO/Mb^*} (%)^b	–	9.1	14.0	15.6	15.5	–	4.5	9.0
final refinement								
R-factor (%)	18.8	18.6	19.8	20.7	20.6	17.1	17.1	19.0
free *R*-factor (%)	25.6	24.6	28.5	29.4	29.2	23.8	23.4	29.6
rmsd from ideal geometry								
bond lengths (Å)	0.012	0.012	0.013	0.013	0.013	0.013	0.014	0.014
bond angles (deg)	1.4	1.5	1.5	1.6	1.5	1.5	1.5	1.7
dihedral angles (deg)	19.0	19.4	19.3	19.6	19.3	19.0	18.8	19.5
improper angles (deg)	1.4	1.5	1.5	1.6	1.6	1.4	1.5	1.6

[a] $R_{merge} = \sum|I - \langle I\rangle|/\sum\langle I\rangle$, where I is the intensity of an observed reflection and $\langle I\rangle$ is the average intensity from multiple observations, including symmetry-related reflections. For Laue data, I is the observed intensity for single reflections normalized by a general scaling factor (Ren & Moffat, 1995a). [b] $R_{MbCO/Mb^*} = \sum|F_{o(MbCO)} - F_{o(Mb^*)}S|/\sum F_{o(MbCO)}$, where $F_{o(MbCO)}$ and $F_{o(Mb^*)}$ are the observed structure factor amplitudes and S is the scaling factor.

values of R_{merge} for the Laue data sets are of concern. However, R_{merge} is an inadequate measure of data quality, particularly for highly redundant data sets (Diederichs & Karplus, 1997), and is also invariably higher for Laue than for monochromatic data (Ren & Moffat, 1995a). Data quality in the present case is better judged by the refinement statistics (Table 2 and Supporting Information).

Structural Refinement. All structural refinement was carried out by the program X-PLOR (Brünger, 1993). For refinement of the two structures based on monochromatic data, MbCO$_M$(40K) and Mb$^*_M$(40K), version 3.0 and the parameter set PARAM19X were used initially. A typical refinement event includes 80–120 positional and 30–50 *B*-factor refinement cycles, in which the number of cycles depends on the resolution. After each event, $|F_o| - |F_c|$, $2|F_o| - |F_c|$, and suitable omit maps were inspected using the program XtalView (McRee, 1992). The model was then manually rebuilt to correct questionable side chains, add or delete solvent molecules, or insert alternate side chain conformations. The rebuilt model was used to initiate a new refinement event. The refinement started with data from the 10–2 Å resolution range. The starting model for the MbCO$_M$(40K) refinement was the 1.6 Å MbO$_2$ single conformation structure at 260 K (Phillips, 1980),[3] from which ligand and solvent molecules had been removed. After four refinement events, the CO ligand was built in; two more refinement events yielded a 2 Å MbCO$_M$(40K) model which served as a starting point for the refinement of the Mb$^*_M$(40K) structure. To prevent possible model bias, the starting model for Mb$^*_M$(40K) excluded the heme, ligand, and seven side chains, those of residues Leu 29, Arg 45, Phe 46, His 64, Thr 67, His 93, and Ile 107, where the most prominent structural differences are observed between the MbCO(260K) and deoxy-Mb structures (Kuriyan et al., 1986; Takano, 1977b; Phillips, 1981). Refinement of Mb$^*_M$(40K) first involved six refinement events similar to those for MbCO$_M$(40K). At this point, X-PLOR 3.1 and the PARHCSDX parameter set (Engh & Huber, 1991) were substituted, augmented by a heme parameter set developed from small molecule data (Lancaster, 1994). Further refinements of both structures were performed in a parallel fashion. We deliberately conducted the crystallographic refinement of the MbCO and Mb* data sets in an identical manner, to minimize systematic errors arising from, for example, differences in the refinement protocols, constraints, or parameter sets. The angular constraints of CO related to the iron, pyrrole nitrogens, and the imidazole nitrogen of the proximal histidine (His 93) for both structures plus the Fe–C bond for the Mb$^*_M$(40K) were gradually released in the last several events of the 10–2 Å refinement. The resolution was gradually increased to 1.69 Å and finally included all reflections where $F/\sigma(F) > 2$ in the resolution range of 10.0–1.69 Å; these comprise 99.2% of all measured reflections for both data sets. The free *R*-factor test was then set up and individual isotropic *B*-factor refinement incorporated. Water molecules were gradually added to the model during refinement. A water molecule was retained only if it was represented by an electron density of greater than 1σ (3σ on omit maps) at the same location in both MbCO$_M$(40K) and Mb$^*_M$(40K) maps. The final models include 183 water molecules, two sulfate molecules, and five (Glu 4, Val 21, Gln 26, Arg 31, and Leu 61) alternate side chain conformations. To simulate the met-Mb content, a water molecule was modeled at the ligand binding site with an initial geometry derived from the met Mb coordinates (Takano, 1977a) and refined as an "alternate conformation" of the CO ligand at the last stage of refinement.

For refinement of structures based on Laue data, the identical refinement program and parameters were used. The refined structures of MbCO$_M$(40K) and Mb$^*_M$(40K) without alternate side chain conformations served as starting models for refinement of MbCO$_L$(40K) and all five Mb$^*_L$ structures. Refinement proceeded through the identical events described above, first from 10 to 2 Å and then expanded to 10–1.8 Å [except for Mb$^*_L$(20K)], without model rebuilding. Table 2 shows the final refinement statistics, which suggest that the structures fall into three levels of quality: excellent [MbCO$_M$(40K) and Mb$^*_M$(40K)], very good [MbCO$_L$(40K), Mb$^*_{L0}$(40K), and Mb$^*_{L1}$(40K)], and good [Mb$^*_{L2}$(40K), Mb$^*_{L3}$(40K), and Mb$^*_L$(20K)]. Further tables that list data reduction and refinement statistics versus resolution for each data set/structure are attached as Supporting Information.

RESULTS

Optical Studies

Figure 2 shows the optical density change of a typical single crystal of MbCO as a function of laser illumination

---

[3] The nomenclature used for the stereochemistry of heme and its ligand is that adopted by the PDB (Bernstein et al., 1977). Quoted structures from the PDB are as follows: Mb$^*_S$(20K), 1ABS in January 1997 (Schlichting et al., 1994); MbCO(260K), 1MBC in September 1988 (Kuriyan et al., 1986); MbO$_2$ 1MBO and R1MBOSF in August 1981 (Phillips, 1980); met-Mb, 4MBN and R4MBNSF in January 1988 (Takano, 1977a); and deoxy-Mb, 5MBN and R5MBNSF in January 1988 (Takano, 1977b) and 1MBD in August 1981 (Phillips, 1981).

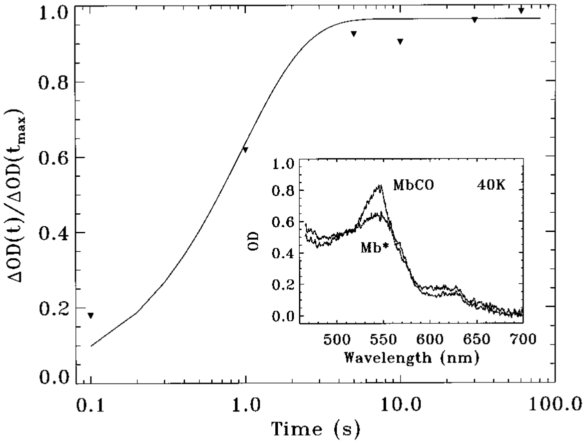

FIGURE 2: Extent of photolysis of a typical MbCO crystal as a function of laser illumination time. The solid line is an exponential fit of the data with a photolysis rate of 1 s^{-1}. The inset shows MbCO and Mb* absorption spectra for the crystal used for monochromatic X-ray data collection at 40 K. Photolysis conditions were the same as those employed during the actual X-ray data collection. The noise in the spectra results from minimizing the monitoring light intensity and exposure time to avoid photolysis by the monitoring beam at these low temperatures, where ligand rebinding kinetics are very slow.

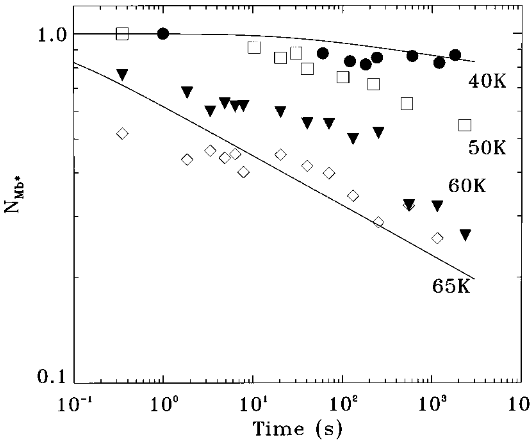

FIGURE 3: Ligand rebinding kinetics in MbCO crystals and frozen solution at low temperatures. The fraction of photoproduct, Mb*, is shown as a function of time on a log−log plot. The discrete symbols are measured data from a crystal; solid lines are fit to solution data from Austin et al. (1975) and correspond to 40 and 65 K. Crystal and solution data both exhibit power law behavior.

time, at a laser power density of 10 mW/mm^2 at 633 nm. At this power density, the photolysis rate was ∼1 s^{-1} and thus an illumination time sufficient to reach a steady state (shown as a saturation of the optical density change in Figure 2) was on the order of a few seconds. With similar experiments in which the laser power density was varied (data not shown), we determined that, under illumination at 10 mW/mm^2, the steady state corresponds to full photolysis at 40 K.

The inset in Figure 2 shows absorption spectra of the crystal used in monochromatic X-ray data collection at 40 K. Features at 630 and 500 nm in these spectra indicate the presence of met-Mb due to incomplete initial reduction of the crystal. The fraction of met-Mb was estimated to be 30%. Similar measurements found the met-Mb content to be <5 and ∼10% for the crystals used for Laue data collection at 40 and 20 K, respectively. The photoproduct spectrum shown in the insert was obtained using the same photolysis protocol employed during the monochromatic X-ray diffraction data collection.

Figure 3 presents ligand rebinding kinetics in MbCO crystals at several cryogenic temperatures. During the monochromatic X-ray exposure of 3 min at 40 K, at most 20% of photodissociated CO ligands recombined with the heme; for Laue data collection with an exposure time on the order of 10 ms, recombination of CO is negligible (<1%). Figure 3 also shows for comparison ligand rebinding kinetics of MbCO in frozen solution (Austin et al., 1975). The kinetic behavior of MbCO crystals at low temperatures is clearly very similar to that of a frozen solution. The additional conformational restraints imposed by the crystal lattice do not significantly affect the ligand rebinding kinetics at low temperatures.

Crystallographic Studies

1. Trajectory of the Photodissociated CO Molecule. Table 3 lists the CO geometry of the MbCO and Mb* structures. We initially reported (Teng et al., 1994a) that the center of the CO molecule is displaced between the bound [MbCO$_M$(40K)] and photolyzed [Mb$^*_M$(40K)] structures by 1.2 Å. The Laue data reveal that, shortly after initiating photolysis, the displacement of CO from its binding site is as short as 0.9 Å in the case of Mb$^*_{L0}$(40K), while after several hours of continuous illumination, the displacement increases to 2.5 Å in the case of Mb$^*_{L3}$(40K). In Mb$^*_M$(40K), Mb$^*_L$(20K), Mb$^*_{L1}$(40K), and Mb$^*_{L2}$(40K), the position of the CO molecule lies between these two extremes (see Table 3). Figure 4 illustrates this positional displacement as a drift or migration of the unbound, photodissociated CO molecule in the heme pocket.

The electron density map of MbCO$_L$(40K) shows well-defined density for bound CO with a peak height of 2.1 e/Å^3 and low *B*-factors for both the C and O atoms of 7.6 and 9.5 Å^2, respectively. The maps for the four Mb$^*_L$(40K) photoproducts also show well-defined density for photodissociated CO with the peak height between 1.6 and 2.1 e/Å^3 with a mean of 1.9 e/Å^3. The *B*-factors for the C and O atoms vary between 7.2 and 9.5 Å^2 with a mean of 8.3 Å^2 and 10.1 and 15.4 Å^2 with a mean of 12.5 Å^2, respectively. The integrated CO electron content is between 9.8 and 13.6 e which corresponds to an occupancy of 70−97% with an estimated error on each value of ±15% (Table 3). This high occupancy confirms our observation by optical measurement of both complete initial photolysis and negligible CO rebinding during the X-ray data collection as well as negligible crystal heating arising from X-ray absorption in our experiment. The high occupancy also suggests that there are no other significantly populated CO site(s) present. The rounded shape of the electron density in the MbCO(40K) maps makes it difficult to accurately determine θ, β, and ϕ angles.[4] In contrast, the elongated electron density which represents the photodissociated CO molecule in the Mb*

---

[4] The CO angular coordinates are defined as follows. The bend angle θ is defined as the Fe−C−O angle. The tilt angle β is defined as the angle between the Fe−C bond and the heme plane normal. The angle between the C−O bond and the heme normal is defined as the angle between the heme normal vector (directed toward the distal pocket) and the vector along the C−O bond, directed from the atom closer to the heme normal to the farther one. The azimuthal angle ϕ (NC−Fe−C−O) is defined as the angle between the plane NC−Fe−C and the plane Fe−C−O. The positive direction of ϕ is defined when the plane Fe−C−O rotates from the NC−Fe−C plane to the ND−Fe−C plane. The heme plane or mean heme plane is defined as the least-squares-fitted plane of the 24 porphyrin core atoms. The nitrogen plane or pyrrole nitrogen plane is defined as the least-squares-fitted plane of the 4 pyrrole nitrogens.

Table 3: CO and Heme Geometry[a]

	$\mathrm{Mb}^*_{\mathrm{L0}}$(40K)	$\mathrm{Mb}^*_{\mathrm{L1}}$(40K)	$\mathrm{Mb}^*_{\mathrm{L2}}$(40K)	$\mathrm{Mb}^*_{\mathrm{L3}}$(40K)	$\mathrm{Mb}^*_{\mathrm{M}}$(40K)	$\mathrm{Mb}^*_{\mathrm{L}}$(20K)	$\mathrm{Mb}^*_{\mathrm{S}}$(20K)	$\mathrm{Mb}^*_{\mathrm{H}}$(20K)	$\mathrm{MbCO}_{\mathrm{M}}$(40K)	$\mathrm{MbCO}_{\mathrm{L}}$(40K)	MbCO(260K)	deoxy-Mb
distances (Å)												
C−O	1.20	1.25	1.21	1.24	1.21	1.20	1.12	1.18/1.18	1.13	1.14	1.17/1.20	−
Fe−C	2.79	3.14	3.53	3.76	2.85	3.10	3.60	2.27/3.71	1.89	1.90	1.92	−
Fe−O	3.53	4.18	4.50	4.70	3.79	3.97	4.14	3.08/4.72	2.91	2.97	2.93	−
⟨Fe−Np⟩	2.00	2.00	2.00	2.00	2.01	1.99	1.98	1.96	2.00	2.01	1.97	2.07
Fe−NE2(93)	2.10	2.20	2.18	2.19	2.11	2.25	2.25	2.21	2.11	2.12	2.19	2.17
C−NE2(64)	3.09	3.88	4.47	4.32	3.40	3.67	3.90	2.93/4.37	3.18	3.31	3.20	−
4-porphyrin nitrogen plane												
Fe−plane	0.09	0.09	0.09	0.11	0.09	0.08	0.19	0.15	0.02	0.02	0.000	0.28
NE2(93)−plane	2.19	2.29	2.27	2.29	2.20	2.32	2.43	2.35	2.13	2.14	2.19	2.44
24-atom heme mean plane												
rms deviation	0.07	0.08	0.09	0.08	0.08	0.06	0.07	0.08	0.07	0.07	0.09	0.07
Fe−plane	0.14	0.14	0.14	0.16	0.15	0.10	0.27	0.23	0.06	0.04	0.04	0.38
C−plane	2.50	2.57	2.69	2.87	2.46	2.62	2.97	2.01/2.99	1.81	1.84	1.88	−
NE2(93)−plane	2.24	2.34	2.31	2.34	2.26	2.33	2.51	2.40	2.17	2.16	2.22	2.54
angles (deg)												
Fe−C−O (θ)	120	141	137	134	134	129	111	123/144	148	155	141/120	−
NC−Fe−C−O (ϕ)	−37	−29	−35	−25	−39	−36	−40	−32/−21	9	39	60/−62	−
NA−Fe−NE2−CE1(93)	1	12	10	11	7	4	12	5	3	2	−10	−4
4-porphyrin nitrogen plane												
Fe−C bond to plane normal	19	29	36	35	22	23	24	9/28	6	6	1	−
NE2(93)−Fe to plane normal	2	3	4	5	2	6	4	2	2	3	3	5
24-atom mean heme plane												
C−O bond to plane normal	70	68	77	81	66	76	91	60/66	39	31	40	−
Fe−C bond to plane normal (β)	19	30	37	36	24	29	26	12/30	8	7	3	−
NE2(93)−Fe to plane normal	3	4	5	5	3	6	3	8	4	5	6	6
CO occupancy (%)	96	97	70	74		87			−	−	−	−

[a] See the text, Figure 1, and footnotes 2 and 3 for the definition of structures in this work and other reference structures; $\mathrm{Mb}^*_{\mathrm{S}}$(20K)and $\mathrm{Mb}^*_{\mathrm{H}}$(36K) are from Schlichting et al. (1994) and Hartmann et al. (1996), respectively. CO in MbCO(260K) and $\mathrm{Mb}^*_{\mathrm{H}}$(36K) structures is modeled with two conformations.

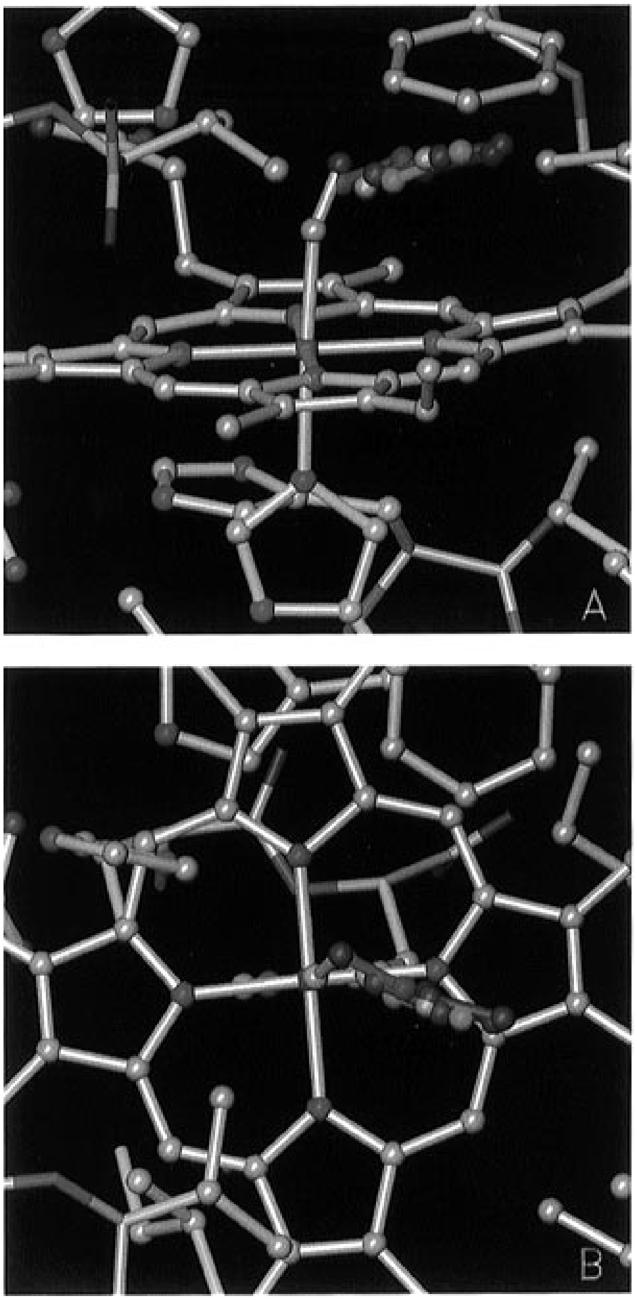

FIGURE 4: Illustration of CO migration. Different CO conformations refined from Laue and monochromatic data are shown with the $\mathrm{MbCO_L}$(40K) model. The photodissociated CO molecules are presented as follows: green, $\mathrm{Mb}^{*}_{\mathrm{L0}}$(40K); yellow, $\mathrm{Mb}^{*}_{\mathrm{M}}$(40K); violet-red, $\mathrm{Mb}^{*}_{\mathrm{L}}$(20K); cyan, $\mathrm{Mb}^{*}_{\mathrm{L1}}$(40K); purple, $\mathrm{Mb}^{*}_{\mathrm{L2}}$(40K); and red, $\mathrm{Mb}^{*}_{\mathrm{L3}}$(40K). (A) Side view and (B) top view of the heme plane.

maps can be fitted with well-defined θ, β, and ϕ angles. These angles are consistent for all six photoproduct structures presented here. θ varies between 120 and 141° with a mean of 133°. β varies between 19 and 37° with a mean of 29°. ϕ varies between -25 and $-39°$ with a mean of $-34°$. The photodissociated CO molecules are therefore nearly parallel to the heme plane, and the angle between the C$-$O bond and the heme normal lies between 68 and 81° with a mean of 73° (see Table 3 and Figure 4).

The above paragraph assumes that the C atom of the photodissociated CO molecule remains closer to the iron atom. We proposed (Teng et al., 1994a) that the CO molecule might have flipped upon photolysis so that its O atom points toward and is closer to the iron atom. (The X-ray data alone cannot distinguish these two orientations.) To explore further the possibility of a flipped CO, we calculated the van der Waals energy for our $\mathrm{Mb}^{*}_{\mathrm{M}}$(40K) structure with the CO molecule both in its original and in its flipped orientation and found that the latter is lower in energy than the former by 1.6 kcal/mol.

We began our refinement of the photodissociated CO molecule by assuming that it adopted a single position and orientation as described above. This is not a unique representation of the data. Figure 5 shows $|F_o - F_c|$ omit maps of $\mathrm{M}^{*}_{\mathrm{L}}$ data, each phased by its own refined structure with the CO omitted. The maps show either a dense core where the refined CO is located plus a "tail", as in $\mathrm{Mb}^{*}_{\mathrm{L0}}$(40K), $\mathrm{Mb}^{*}_{\mathrm{M}}$(40K), $\mathrm{Mb}^{*}_{\mathrm{L2}}$(40K), and $\mathrm{Mb}^{*}_{\mathrm{L3}}$(40K) or an elongated electron density with a core in the middle and reduced density on both ends, as in $\mathrm{Mb}^{*}_{\mathrm{L}}$(20K) and $\mathrm{Mb}^{*}_{\mathrm{L1}}$(40K). We continued refinement of all structures with a two-site CO model, in which one CO site (CO1) was taken from $\mathrm{Mb}^{*}_{\mathrm{L0}}$(40K) and the second (CO2) from $\mathrm{Mb}^{*}_{\mathrm{L3}}$(40K). Upon conclusion of the refinement, CO1 had moved even closer to, and CO2 had moved further from, the bound CO site. The geometry of CO2 was well-defined, whereas the θ and ϕ angles of CO1 were not. A new two-site CO model which averages the CO1 and CO2 coordinates of each $\mathrm{M}^{*}_{\mathrm{L}}$ structure was then employed. With these coordinates fixed, we finally refined the occupancies of the two sites and obtained values for the ratio of the occupancies CO1/CO2 of Mb* structures. Table 4 shows the geometric parameters of the model and refined occupancies, which vary from 60/40 to 34/66 for $\mathrm{Mb}^{*}_{\mathrm{L0}}$(40K) and $\mathrm{Mb}^{*}_{\mathrm{L3}}$(40K) respectively. That is, there is a progressive decrease in the occupancy of the CO1 site and a parallel increase in that of the CO2 site.

2. Heme Geometry. Our initial report was based on a model refined to 2 Å resolution with the monochromatic X-ray data (Teng et al., 1994a) and revealed only very limited tertiary structural changes in the heme and globin upon MbCO photolysis. This general conclusion is fully confirmed by our new Laue data, which are unaffected by errors arising from met-Mb content or CO rebinding. Table 3 also lists details of the heme geometry, which is known to change on transition from the ligand-bound, low-spin, six-coordinate structure to the ligand-free, high-spin, five-coordinate structure at room temperature. On ligand photolysis at 40 K, the iron atom moves out of the heme plane by 0.1 Å, which corresponds to ~30% of the full 0.31$-$0.34 Å iron displacement between the deoxy-Mb (Takano, 1977b; Phillips, 1981) and MbCO(260K) (Kuriyan et al., 1986) structures. The iron displacement does not increase further in the photoproduct structures examined after extended illumination (see Table 3).

3. Tertiary Structural Changes after Photolysis. We examined the scatter plots of difference electron density values, $\Delta\rho$, between Mb* and MbCO as a function of the distance from the center of the bound CO molecule (not shown). These plots, which are independent of structural refinement, would reveal how structural changes propagate from the CO binding site through the heme and globin with time. The signal beyond a distance of ~8 Å from the bound CO site cannot be distinguished from noise. Evidently, tertiary structural changes are very small after photolysis of MbCO at these low temperatures.

Positional deviations of those residues which have non-hydrogen atoms within 8 Å of the CO molecule in the two refined structures of $\mathrm{Mb}^{*}_{\mathrm{M}}$(40K) and $\mathrm{MbCO_M}$(40K) were calculated after superimposing the heme planes. The results

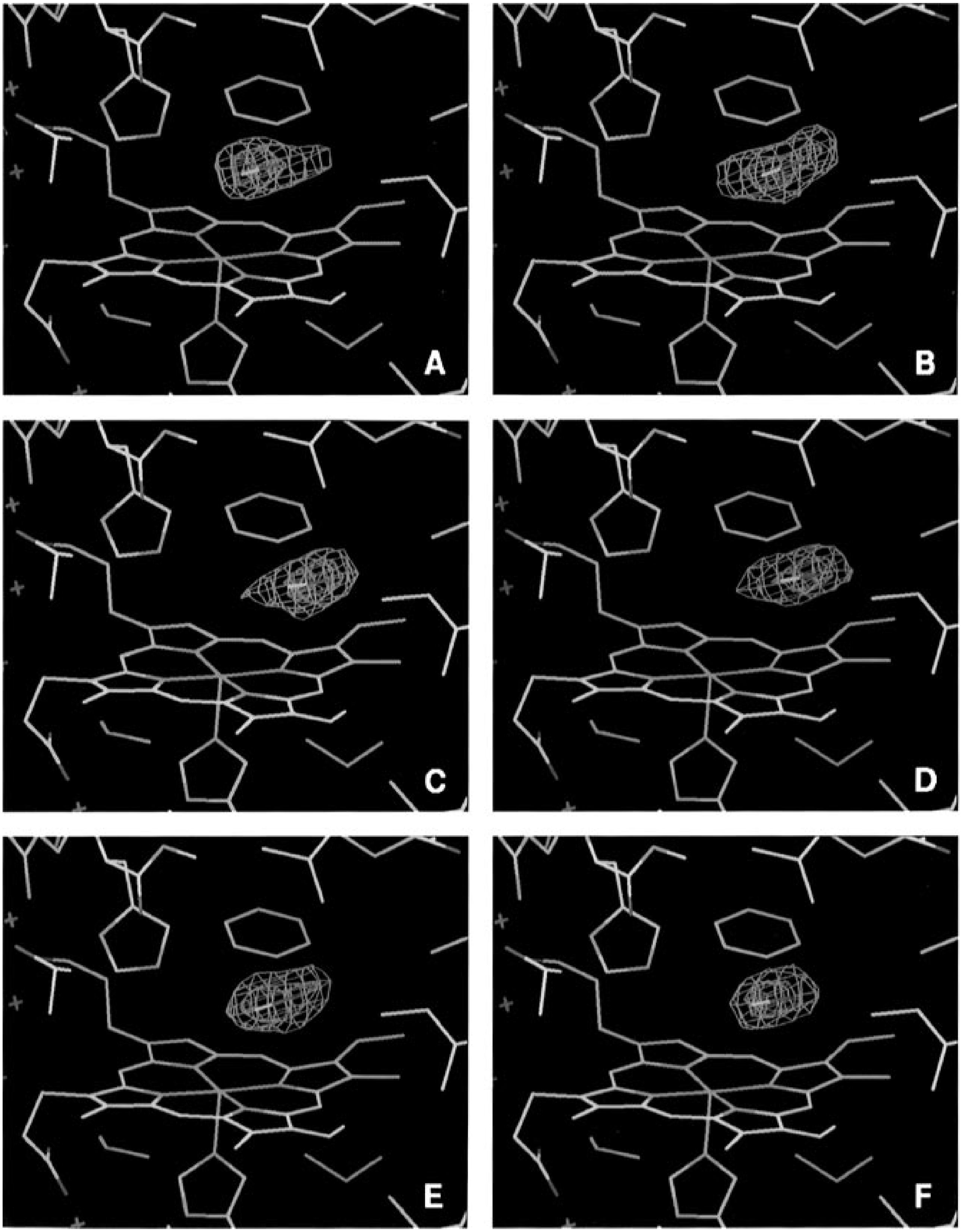

FIGURE 5: Omit CO maps of Mb* structures. $|F_o - F_c|$ difference Fourier maps phased by their refined model with the CO molecule omitted. Contour levels: green, 3σ; and red, 5σ. (A) $\mathrm{Mb}^*_{\mathrm{L0}}$(40K). (B) $\mathrm{Mb}^*_{\mathrm{L1}}$(40K). (C) $\mathrm{Mb}^*_{\mathrm{L2}}$(40K). (D) $\mathrm{Mb}^*_{\mathrm{L3}}$(40K). (E) $\mathrm{Mb}^*_{\mathrm{M}}$(40K). (F) $\mathrm{Mb}^*_{\mathrm{L}}$(20K).

show that the positional shifts between the two structures in the vicinity of the CO molecule are all smaller than 0.13 Å for backbone atoms and 0.14 Å for side chains. We do not observe changes in the geometry of the proximal histidine (His 93) after short illumination, as in the $\mathrm{Mb}^*_{\mathrm{M}}$(40K) structure (see Table 3). There is an indication, however, of an increase in the Fe−NE2(93) bond length and the NA−Fe−NE2−CE1(93) angle after extended illumination, as in the $\mathrm{Mb}^*_{\mathrm{L1}}$(40K), $\mathrm{Mb}^*_{\mathrm{L2}}$(40K) and $\mathrm{Mb}^*_{\mathrm{L3}}$(40K) structures. The rms positional shifts were also calculated for each residue after superimposing the main chain (residues 4−149) atoms of the $\mathrm{MbCO}_{\mathrm{M}}$(40K) and $\mathrm{Mb}^*_{\mathrm{M}}$(40K) structures. All shifts are smaller than 0.08 Å for backbone atoms and 0.25 Å for side chain atoms, except for three residues (Lys 34,

Table 4: Two-Site CO Model

	CO1	CO2
distances (Å)		
C−O	1.11	1.14
Fe−closer atom	2.28	3.94
Fe−more distant atom	3.32	4.83
angles (deg)		
Fe−C−O (θ)	153	136
NC−Fe−C−O (ϕ)	0	−1
occupancy (%)		
$\mathrm{Mb}^*_{\mathrm{L0}}$(40K)	60	40
$\mathrm{Mb}^*_{\mathrm{M}}$(40K)	58	42
$\mathrm{Mb}^*_{\mathrm{L}}$(20K)	54	46
$\mathrm{Mb}^*_{\mathrm{L1}}$(40K)	47	53
$\mathrm{Mb}^*_{\mathrm{L2}}$(40K)	36	64
$\mathrm{Mb}^*_{\mathrm{L3}}$(40K)	34	66

Lys 50, and Lys 87) whose side chain electron densities are too weak to refine well.

Kuriyan et al. (1986) proposed that motion of Arg 45 opens a pathway for ligand entry to and escape from the heme pocket. Later molecular dynamics simulations supported their proposal (Elber & Karplus, 1990). We therefore examined possible alternate conformations of Arg 45. Our $\mathrm{MbCO_M}$(40K) map shows only an indication of the Arg 45 alternate conformation at the 0.6σ contour level. Occupancy of the refined minor conformation is low, 27%, and suggests that the side chain of Arg 45 swings out into the solvent region and opens up the heme pocket. This conformation differs from that of Kuriyan et al. (1986), who suggested that the alternate side chain conformation is buried inside the boundary of the molecule.

We calculated the rms backbone positional shift for each residue when the $\mathrm{MbCO_L}$(40K) and $\mathrm{Mb}^*_{\mathrm{L0}}$(40K) or MbCO(260K) and deoxy-Mb structures are superimposed by their backbone atoms. The overall rms deviation of the least-squares fit is 0.06 Å for the $\mathrm{MbCO_L}$(40K) and $\mathrm{Mb}^*_{\mathrm{L0}}$(40K) structures, compared to 0.24 Å for the MbCO(260K) and deoxy-Mb structures. Clearly, the deviation between the 40 K structures is much smaller than that between the room-temperature structures.

For a global view of structural differences, the matrices of distance differences were plotted. For each structure, a matrix of the distances between the main chain centroid of each residue and the main chain centroid of all other residues is calculated. The matrices of two compared structures are then subtracted to generate a matrix of distance differences. Figure 6 shows these matrices for the structure pairs $\mathrm{MbCO_M}$(40K)−$\mathrm{Mb}^*_{\mathrm{M}}$(40K) and MbCO(260K)−deoxy-Mb, in which the distance difference is color-coded. Two features are apparent. First, the $\mathrm{MbCO_M}$(40K)−$\mathrm{Mb}^*_{\mathrm{M}}$(40K) matrix shows fewer structural differences than its counterpart, the MbCO(260K)−deoxy-Mb matrix. Second, there is little correlation of the largest differences between the $\mathrm{MbCO_M}$(40K)−$\mathrm{Mb}^*_{\mathrm{M}}$(40K) and the MbCO(260K)−deoxy-Mb matrices. Thus, if we assume that the $\mathrm{Mb}^*_{\mathrm{M}}$(40K) structure represents an early stage in the evolution from the ligand-bound $\mathrm{MbCO_M}$(40K) structure to the final, ligand-free, deoxy-Mb structure, it does not develop characteristics of deoxy-Mb to the same extent in all portions of the sequence. For example, among the prominent differences between MbCO(260K) and deoxy-Mb such as those in the CD corner, F helix, and GH loop, significant changes are present only in the CD corner in the $\mathrm{MbCO_M}$(40K)−$\mathrm{Mb}^*_{\mathrm{M}}$(40K) matrix and are essentially absent in the F helix and GH loop.

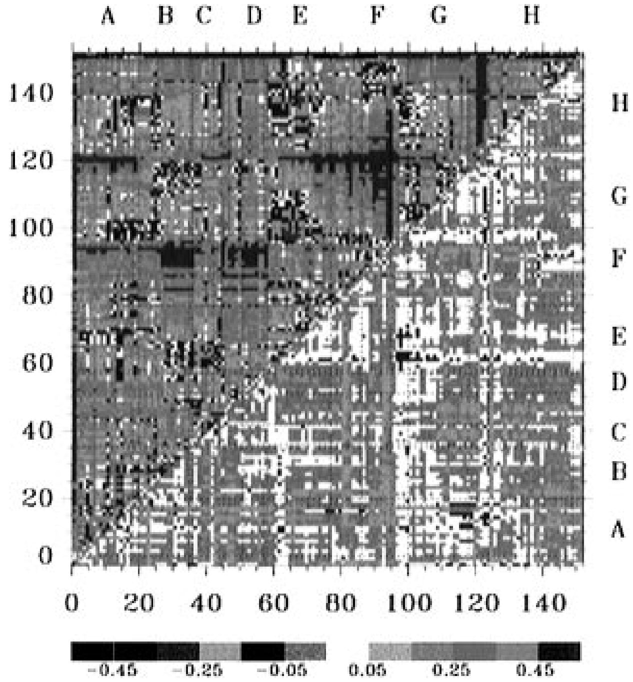

FIGURE 6: Difference distance matrices of backbone centroid. The upper left diagonal part presents the differences between MbCO(260K) and deoxy-Mb structures and the lower right diagonal part for $\mathrm{MbCO_M}$(40K) and $\mathrm{Mb}^*_{\mathrm{M}}$(40K). Differences in the range of 0.05−0.45 Å are coded to four colors with an increment of 0.1 Å; differences beyond that range are treated as two groups with the lightest or darkest color.

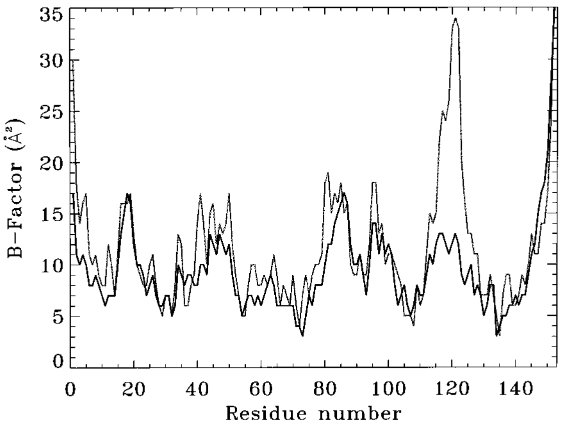

FIGURE 7: Distribution of the average *B*-factor of backbone atoms as a function of residue number: $\mathrm{MbCO_L}$(40K), heavy line; and 300 K MbCO Laue data, light line.

In summary, both the difference electron density maps and the refined structures establish that the myoglobin molecules in the crystal show a relatively rigid structure after photolysis at cryogenic temperatures; little structural relaxation occurs. The structural differences between MbCO(40K) and Mb*(40K) involve displacement of the iron atom out of the heme plane upon photolysis by 0.1 Å. The heme, slightly domed, rotates by 1° about approximately the NB−ND axis. Pyrroles B, C, and D move toward the distal side, while pyrrole A moves in the opposite direction with the largest motion exhibited by pyrrole C. No shifts larger than ∼0.2 Å of any residues surrounding the heme, including the proximal and distal histidines, His 93 and His 64, are observed. The peptide backbone exhibits even smaller changes.

4. Temperature Factors. Figure 7 shows the average *B*-factor of backbone atoms as a function of residue number for the $\mathrm{MbCO_L}$(40K) structure and an MbCO Laue structure determined at 300 K (T.-Y.-Teng, V. Šrajer, and K. Moffat, unpublished). The distributions are very similar in both shape and magnitude; in particular, the *B*-factors at 40 K are not significantly smaller than those at 300 K, except near the GH loop. This is inconsistent with the finding of Parak et al. (1987) which stated that *B*-factors are significantly reduced at 80 K as compared to those at 300 K. It suggests that, with our cooling protocol, the room-temperature disorder is simply "frozen" during the rapid (∼300 K/s) cooling. The substantial reduction at 80 K found by Parak et al. (1987) could result from much slower cooling which allows re-equilibration of the molecular structure and cell dimensions (Teng & Moffat, 1997).

DISCUSSION

Comparison with Room-Temperature Structures

1. Fe−C−O Geometry. Table 3 compares the CO−heme geometry in our structures with that of other reported structures. The Fe−C−O bend angle θ is 150 ± 5° in MbCO(40K), in agreement with X-ray diffraction studies on the monoclinic, $P2_1$ crystal form ($\theta \sim 141°$) (Kuriyan et al., 1986; Hartmann et al., 1996). X-ray diffraction studies of synthetic sperm whale MbCO which crystallize in the hexagonal, *P*6 crystal form indicate a less bent conformation ($\theta \sim 160-170°$) (Quillin et al., 1993; Schlichting et al., 1994). Polarized IR measurements on single crystals in both the monoclinic, $P2_1$, and orthorhombic, $P2_12_12_1$, crystal forms (Ivanov et al., 1994) are consistent with a small bend of the Fe−C−O system, with an angle of $\leq 10°$ between the C−O bond and the heme normal. Photoselection IR measurements in solution (Lim et al., 1995a) also suggest a nearly linear Fe−C−O conformation, with a less than 7° angle between the C−O bond and the heme normal. More work is needed to establish if the differences between different crystal forms and between crystals and solution are real or result from limitations of these experimental techniques and interpretation of their results.

As noted above, the round electron density representing the bound CO molecule suggests that bound CO might be structurally disordered. However, our experiments do not resolve the distinct structural substates of the bound CO molecules suggested by IR and photoselection measurements in solution and referred to as A states (Moore et al., 1988; Ormos et al., 1988), observed also in room-temperature MbCO crystals (Kuriyan et al., 1986). Our inability to structurally resolve A states does agree with other polarized IR measurements on single crystals (Ivanov et al., 1994) and in solution (Lim et al., 1995a) where only a single orientation of the bound CO molecule was observed.

2. Ligand Trajectory. The migration of the photodissociated CO molecule in the heme pocket at cryogenic temperatures is likely to be related to the earliest stages of ligand migration at room temperature in solution and in crystals. Our recent nanosecond time-resolved X-ray diffraction study on photolyzed MbCO crystals at room temperature indicates that, 4 ns after photolysis, a partly occupied, photodissociated CO molecule is located in the ligand pocket [see feature R in Figure 1A of Šrajer et al. (1996)]. The photodissociated CO could not be visualized 1 μs after photolysis, due in part to recombination with the iron and presumably in part to further motion away from the heme through the protein. The CO is therefore displaced by roughly 2 Å/μs at 300 K, in marked contrast to roughly 0.5 Å/h at 40 K in the present study. The velocity at 40 K is a factor of 10^{10} lower than that at 300 K and illustrates the enormous decrease in structure relaxation rates upon cooling. Studies at low temperatures therefore provide a simpler experimental route to the earliest stages of the ligand trajectory.

Does the "dynamic" picture depicted by the low-temperature crystallographic result arise from the drift with time of the centroid of a continuous spatial distribution of CO molecules? Or does it arise from "hopping" of CO molecules between two or more spatially distinct sites? As noted above, modeling of the CO molecule by a single site with an isotropic *B*-factor whose location varies with time does not uniquely represent the omit maps (Figure 5). Representation of photodissociated CO molecule by two discrete sites, CO1 and CO2, whose location remains fixed and whose relative occupancy varies with time provides an alternative representation (Figure 5 and Table 4).

IR measurements in solution (Alben et al., 1982; Lim et al., 1995b) have been interpreted to show that the photodissociated CO molecule adopts several discrete conformations in the heme pocket (referred to as B states) at both low and room temperatures. Although the different frequencies of B states suggest that the photodissociated CO molecules experience a different local environment in each state, the structural differences between them are still not unambiguously determined. Lim et al. (1995a,b, 1997) proposed that two B states, which they denote as B_1 and B_2 and which are populated a few picoseconds after photolysis at room temperature, correspond to the same CO spatial location (a docking site) in the ligand pocket but with opposite C−O orientations. In the more stable B_1 state to which B_2 converts thermally (even at 13 K; Alben et al., 1982), the O atom is directed toward the iron, as proposed by Teng et al. (1994a) and consistent with measurements of the rebinding rates of $^{13}C^{16}O$ and $^{12}C^{18}O$ (Alben et al., 1980). Geminate rebinding of CO from the B_1 state would be greatly hindered relative to that of O_2, since rotation end-for-end of CO, but not of O_2, would be required. Lim et al. (1997) also propose that the photodissociated CO is funneled into this docking site, moving down a potential gradient. The docking site probably corresponds to the CO location nearer to the iron, depicted by the low-temperature crystallography [site CO1 in Table 4; see also Hartmann et al. (1996)].

Geminate rebinding occurs to an incompletely relaxed Mb* state. Similar considerations come into play for the binding of CO to fully relaxed deoxy-Mb, in a bimolecular reaction. If the structure of the relaxed ligand pocket and heme energetically favor presentation of the O of CO to the iron rather than to C, then binding of CO is disfavored relative to that of O_2.

Comparison with Computational Studies

Very recently, Vitkup et al. (1997) reported molecular dynamics simulations of solvated, photodissociated myoglobin at room temperature, based on 28 independent trajectories spanning 10 ps and utilizing the room-temperature MbCO structure of Kuriyan et al. (1986). Data from all trajectories were combined to construct a probability distribution for photodissociated CO in the ligand pocket. This distribution becomes independent of time in less than 1 ps, but no data were presented on the time course with which the distribution was established. We superimpose our

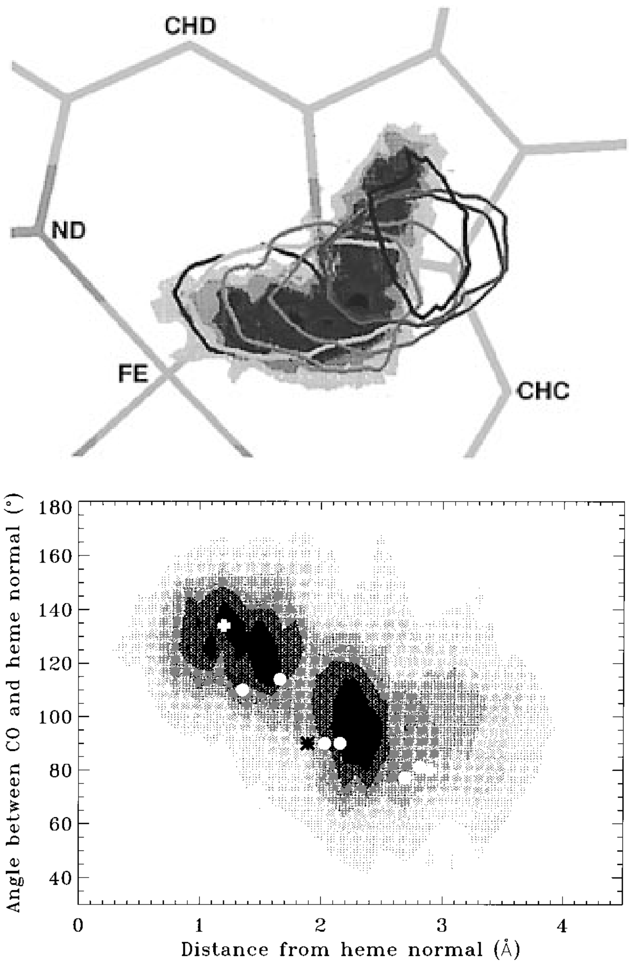

FIGURE 8: Crystallographic results of this work overlaid on the theoretical CO probability distributions of Vitkup et al. (1997). (A, top) CO electron density of the F_o maps of Mb* overlaid on Figure 2 of Vitkup et al. (1997). The color code for electron density contours is as follows: green, $\mathrm{Mb}^*_{\mathrm{L0}}$(40K); yellow, $\mathrm{Mb}^*_{\mathrm{M}}$(40K); violet-red, $\mathrm{Mb}^*_{\mathrm{L}}$(20K); cyan, $\mathrm{Mb}^*_{\mathrm{L1}}$(40K); purple, $\mathrm{Mb}^*_{\mathrm{L2}}$(40K); red, $\mathrm{Mb}^*_{\mathrm{L3}}$(40K); and blue, room-temperature Mb* (Šrajer et al., 1996). The electron densities are displayed at the 2.5 σ level except for the room-temperature data, which is contoured at 1σ. (B, bottom) CO locations of Mb* structures overlaid on Figure 3 of Vitkup et al. (1997). The angles between CO and the heme normal are presented according to the definition of Vitkup et al. [see the legend to Figure 3 in Vitkup et al. (1997)], assuming that the O atom is closer to the iron at the site CO1. Their definition differs from ours (see footnote 4). For the single-site model, structures are assumed to have the O atom closer to the iron if CO1 occupancy is ≥60% [i.e., $\mathrm{Mb}^*_{\mathrm{L0}}$(40K) and $\mathrm{Mb}^*_{\mathrm{M}}$(40K)] or the C atom closer to the iron if CO2 occupancy is ≥60% [i.e., $\mathrm{Mb}^*_{\mathrm{L2}}$(40K) and $\mathrm{Mb}^*_{\mathrm{L3}}$(40K)] and a mix of 50% of each if the occupancy ratio CO1/CO2 is close to 1.0 [i.e., $\mathrm{Mb}^*_{\mathrm{L}}$(20K) and $\mathrm{Mb}^*_{\mathrm{L1}}$(40K)]. Circle, single-site model; cross, two-site model; and asterisk, $\mathrm{Mb}^*_{\mathrm{S}}$(20K) structure of Schlichting et al. (1994).

experimental results at both cryogenic and room temperature (Šrajer et al., 1996) on their time-independent theoretical probability distributions in Figure 8. The agreement is excellent between these completely independent studies; the experimental locations (Figure 8A) and orientations (Figure 8B) of the photodissociated CO follow very closely the theoretical distributions. This supports three ideas. (1) The trajectories at low temperatures may be identified with the earliest stages of the trajectories at room temperature. (2) Initial migration of photodissociated CO takes place within a largely unrelaxed, MbCO-like structural framework as our crystallographic results indicate. (3) In the CO1 location, the CO has flipped and the O atom is closer to the heme normal and the iron, but in the CO2 location, the C atom is closer to the heme normal and the iron. The close match between the 2.5σ contour in the F_o maps representing the photodissociated CO and the 150-event contour from the probability distribution suggests that, at least in this example, experimental studies have revealed mobile CO quite accurately. It would be of considerable interest to extend the computational studies to longer time domains that would explore later stages in the ligand trajectories, and to parallel these with experimental studies.

Comparison with Other Low-Temperature Structures of the Photoproduct

Schlichting et al. (1994) investigated the photoproduct structure at 20 K with the hexagonal, *P*6 crystal form, which we denote as $\mathrm{Mb}^*_{\mathrm{S}}$(20K). They found the photodissociated CO molecule to be ~2 Å from its binding site, with an Fe−C distance of 3.6 Å and the CO molecule parallel to the heme plane making a 91° angle between the CO bond and the heme normal. They estimated the movement of iron out of the heme plane to be 0.22 Å, corresponding to 70% of the 0.31−0.34 Å change between MbCO (Kuriyan et al., 1986) and deoxy-Mb (Takano, 1977b; Phillips, 1981). They also observed large conformational changes in the side chains of the heme pocket, especially for His 64 and Arg 45. Indeed, the displacement of His 64 is very large and, unexpectedly, in the opposite direction with respect to that between MbCO and deoxy-Mb.

Recently, Hartmann et al. (1996) investigated the photoproduct structure at 36 K on the monoclinic, $P2_1$ crystal form grown at pH 6.2, which we denote as $\mathrm{Mb}^*_{\mathrm{H}}$(36K). The electron density representing the photodissociated CO could not be modeled by a single site. A two-site CO model placed one site far from the bound CO location with an Fe−C distance of 3.7 Å and a second very close to the bound location with an Fe−C distance of 2.27 Å, which they interpreted as rebound CO (although this distance is too long for a covalent bond; Vitkup et al., 1997). They also report a value of 0.15 Å for the iron displacement from the mean heme plane, which corresponds to complete iron relaxation if 42% CO rebinding is assumed or 50% relaxation if no rebinding is assumed. However, they did not observe the large displacement of the distal histidine reported by Schlichting et al. (1994), or other large conformational changes.

These structural results (Schlichting et al., 1994; Hartmann et al., 1996) differ quantitatively from our earlier report (Teng et al., 1994a). We observed a nearby but different location for photodissociated CO and only about 30% of the iron movement. The three experiments differ in several key aspects: crystal form, pH, cooling protocol, final temperature, illumination/photolysis protocol, and X-ray data collection protocol. Which aspect(s) accounts for the real structural differences among them? As noted above, our new Laue data for $\mathrm{Mb}^*_{\mathrm{L0}}$(40K), acquired with the photolysis protocol identical to that used for $\mathrm{Mb}^*_{\mathrm{M}}$(40K), resulted in an effectively identical photoproduct structure. The differences therefore cannot be attributed to the higher content of met-Mb or of rebound CO in our earlier $\mathrm{Mb}^*_{\mathrm{M}}$(40K) structure.

Although protein is expected to be very rigid in both monoclinic and hexagonal crystal forms at low temperatures, the very substantial transient heating caused by photon absorption (Henry et al., 1986) may cause relaxation to a

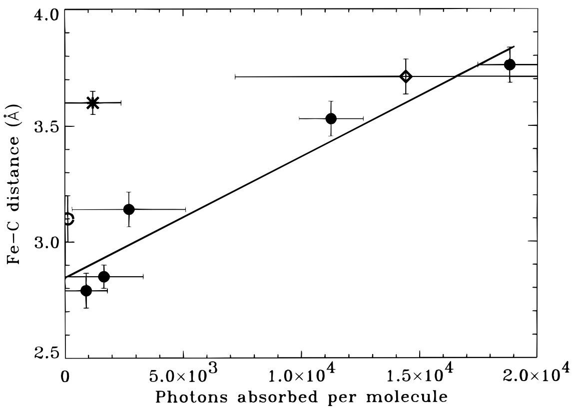

FIGURE 9: Drift of the photodissociated CO molecule under extended illumination. The Fe−C distance in Mb* structures is plotted as a function of the total number of photons absorbed per molecule, which is calculated by multiplication of the total illumination time and the photolysis rate (assuming a quantum yield of 1). A photolysis rate of 2 s^{-1} was chosen for Hartmann et al. (1996) (who estimated a range of 1−10 s^{-1}) and 0.3 s^{-1} for Schlichting et al. (1994) (who estimated a range of 0.003−0.3 s^{-1}). The horizontal error bars extend from the beginning to the end of the X-ray data acquisition; the vertical error bars are assigned to reflect the resolution of refined structures. Black circle, 40 K data; open circle, 20 K data of this work; asterisk, Mb^*_S(20K); and diamond, Mb^*_H(36K). The line is a simple linear fit.

different extent in the two crystal forms and hence in our three experiments. This is the main reason for restricting the total number of photons absorbed by the crystal to that required for photolysis (Figure 2). Both Schlichting et al. (1994) and Hartmann et al. (1996) collected their X-ray data under continuous light illumination. However, our Laue experiments here show that extended illumination at these light intensities does influence the structural results. Figure 9 presents the CO displacement as a function of the total number of photons absorbed per myoglobin molecule, for both their experiments and ours. It shows clearly that photodissociated CO drifts with time when the laser illumination is continuous even under conditions of weak illumination. After more than 5 h of illumination, we find that the CO molecule is located even farther from the heme than Schlichting et al. (1994) and Hartmann et al. (1996) observed it to be.

It therefore appears that different photolysis protocols are mainly responsible for the different CO locations observed in the three earlier experiments. Our present time-resolved results encompass all the earlier, static CO locations. The remaining structural differences may arise from the different crystal forms which differ in their dynamic properties at room temperature (Phillips, 1990); from variation in the met-Mb content and the extent of CO rebinding, both of which require on-line single-crystal microspectroscopy for accurate evaluation and are therefore uncertain in the Schlichting et al. (1994) and Hartmann et al. (1996) structures; and possibly from brief, undetected temperature jumps which are likely unless the cryosystem is carefully designed and operated. Such jumps would greatly promote structural relaxation. The last might account for the extensive and unusual tertiary structural changes seen by Schlichting et al. (1994) which are absent in our attempt to replicate their experiment in our Mb^*_L(20K) data.

Light-Induced Relaxation

What causes the observed slow CO drift under continuous illumination? Is it caused by repeated local, transient heating of the heme environment upon absorption of a photon (Henry et al., 1986) during the extended illumination? Or does extended illumination serve merely to keep the CO dissociated and thus increase its chance to drift away and to populate longer-lived conformational substates (Ansari et al., 1987)? Our Laue data at 20 K indicate that the second effect might be important, although it is likely that both effects contribute. At 20 K, after only a short illumination of 120 s, the CO ligand is located further from the heme than after 60 min of illumination at 40 K (Table 1 and 3). Since in our experiment the time and illumination variables are confounded, new experiments are need to answer these questions.

Studies of frozen solutions and room-temperature crystals demonstrate that extended illumination and higher light intensities dramatically alter the rebinding kinetics in MbCO, by several orders of magnitude (Powers et al., 1987; Šrajer et al., 1991; Nienhaus et al., 1992, 1994; Zhu et al., 1993). The origin of this prominent, light-induced relaxation has been in doubt. Nienhaus et al. (1994) observed that, after extended illumination, the frequencies of the IR bands associated with photodissociated CO do not exhibit a significant shift when monitored via temperature derivative spectroscopy, but that the frequency of the near-IR band III in photodissociated myoglobin [which is believed to be sensitive to the detailed structure of the five-coordinate iron (Iizuka et al., 1974)] did shift. They therefore attribute the effect of extended illumination to a light-induced relaxation of the heme and the protein, similar but not completely equivalent to thermal relaxation and whose extent is proportional to the number of photons absorbed. They rule out light-induced motion of the CO to other site(s) in the ligand pocket. In contrast, Powers et al. (1987) and Šrajer et al. (1991) attribute the effects to ligand drift to a more distant, less accessible site in the heme pocket. Our results support the latter suggestion, that the major effect of continuous illumination is induction of CO drift or migration rather than heme and globin relaxation. We see clear migration of the photodissociated CO upon continuous illumination, but the iron displacement remains at ~0.1 Å in all photoproduct structures. However, there is an indication of small, progressive structural changes on the proximal side of the heme during continuous illumination, consistent with resonance Raman measurements (Ahmed et al., 1991) that report a change in intensity of the iron−proximal histidine stretch band at ~230 cm^{-1} in Mb* after extended illumination. The proximal changes involved may also result in the shift of band III. The absence of the frequency shift of the IR bands under continuous illumination (Nienhaus et al., 1994) is consistent with the two-site description of our data, in which the locations of the two sites are fixed but their relative population changes under continuous illumination. In this model, the photodissociated CO is hopping from the closer (CO1) to the farther (CO2) location in the heme pocket. The two-site model is also consistent with the molecular dynamics simulations of Vitkup et al. (1997) that indicate the existence two high-probability sites in the heme pocket for photodissociated CO. Finally, we note that, in agreement with Nienhaus et al. (1994), the extent of light-induced relaxation is proportional to the number of photons absorbed (Figure 9).

In conclusion, our studies of MbCO photolysis by continuous light illumination at cryogenic temperatures reveal a more complete ligand trajectory than previous partial studies (Teng et al., 1994; Schlichting et al., 1994; Hartmann et al., 1996). The photodissociated CO molecule drifts slowly, and its displacement from the binding site increases from 0.9 to 2.5 Å. The results can also be described by a two-site model in which the distances to the iron atom are 2.8 and 4.4 Å for the near site (CO1) and farther site (CO2), respectively. The atom closer to the iron and heme is O for the near site and C for the farther site. Their relative populations change with time and light illumination, which can be depicted as the species in site CO1 hopping to site CO2 under continuous illumination. These two sites are consistent with two higher-probability regions for the photodissociated ligand predicted by molecular dynamics simulations.

ACKNOWLEDGMENT

We thank Wladek Minor for advice on using the DENZO program, Duncan McRee for providing his XtalView program prior to its release, Roy Lancaster for his heme parameter set, Zhong Ren and Chris Dealwis for many helpful discussions and suggestions on crystallographic data reduction and refinement, Ying Chen, Alan LeGrand, Grace Shea McCarthy, Kingman Ng, Claude Pradervand, Mark Rivers, and Wilfried Schildkamp for their valuable assistance in designing and constructing the apparatus essential for these experiments and in data collection, Martin Karplus for commenting on the manuscript, Dennis Vitkup for providing original figures, and Fritz Parak for the $\mathrm{Mb}^*_{\mathrm{H}}$(36K) coordinates.

SUPPORTING INFORMATION AVAILABLE

Two tables with more detailed statistics of X-ray data reduction and structural refinement (2 pages). Ordering information is given on any current masthead page.

REFERENCES

Ahmed, A. M., Campbell, B. F., Caruso, D., Chance, M. R., Chavez, M. D., Courtney, S. H., Friedman, J. M., Iben, I. E. T., Ondrias, M. R., & Yang, M. (1991) *Chem Phys. 158*, 329−351.

Alben, J. O., Beece, D., Bowne, S. F., Eisenstein, L., Frauenfelder, H., Good, D., Marden, M. C., Moh, P. P., Reinisch, L., Reynolds, A. H., & Yue, K. T. (1980) *Phys. Rev. Lett. 44*, 1157−1160.

Alben, J. O., Beece, D., Bowne, S. F., Doster, W., Eisenstein, L., Frauenfelder, H., Good, D., McDonald, J. D., Marden, M. C., Moh, P. P., Reinisch, L., Reynolds, A. H., Shyamsunder, E., & Yue, K. T. (1982) *Proc. Natl. Acad. Sci. U.S.A. 79*, 3744−3748.

Ansari, A., Berendzen, J., Bowne, S. F., Frauenfelder, H., Iben, I. E. T., Sauke, T. B., Shyamsunder, E., & Young, R. D. (1985) *Proc. Natl. Acad. Sci. U.S.A. 82*, 5000−5004.

Ansari, A., Berendzen, J., Braunstein, D., Cowen, B. R., Frauenfelder, H., Hong, M. K., Iben, I. E. T., Johnson, J. B., Ormos, P., Sauke, T. B., Scholl, R., Schulte, A., Steinbach, P. J., Vittitow, J., & Young, R. D. (1987) *Biophys. Chem. 26*, 337−355.

Austin, R. H., Beeson, K. W., Eisenstein, L., Frauenfelder, H., & Gunsalus, I. C. (1975) *Biochemistry 14*, 5355−5373.

Bernstein, F. C., Koetzle, T. F., Williams, G. J. B., Meyer, E. F., Jr., Brice, M. D., Rodgers, J. R., Kennard, O., Shimanouchi, T., & Tasumi, M. (1977) *J. Mol. Biol. 112*, 535−542.

Brünger, A. T. (1993) *X-PLOR version 3.1, A system for X-ray crystallography and NMR*, Yale University Press, New Haven, CT.

Carver, T. E., Brantley, R. E., Jr., Singleton, E. W., Arduini, R. M., Quillin, M. L., Phillips, G. N., Jr., & Olson, J. S. (1992) *J. Biol. Chem. 267*, 14443−14450.

Case, D. A., & Karplus, M. (1979) *J. Mol. Biol. 132*, 343−368.

CCP4 (1979) *The SERC (UK) Collaborative Computing Project #4. A Suite of Programs for Protein Crystallography*, Daresbury Laboratory, Warrington, England.

Chen, Y., Šrajer, V., Ng, K., LeGrand, A., & Moffat, K. (1994) *Rev. Sci. Instrum. 65*, 1506−1511.

Diederichs, K., & Karplus, P. A. (1997) *Nat. Struct. Biol. 4*, 269−275.

Elber, K., & Karplus, M. (1990) *J. Am. Chem. Soc. 112*, 9161−9175.

Engh, R. A., & Huber, R. (1991) *Acta Crystallogr. A47*, 392−400.

Hartmann, H., Zinser, S., Komninos, P., Schneider, R. T., Nienhaus, G. U., & Parak, F. (1996) *Proc. Natl. Acad. Sci. U.S.A. 93*, 7013−7016.

Henry, E. R., Eaton, W. A., & Hochstrasser, R. M. (1986) *Proc. Natl. Acad. Sci. U.S.A. 83*, 8982−8986.

Huang, X., & Boxer, S. G. (1994) *Nat. Struct. Biol. 1*, 226−229.

Iizuka, T., Yamamoto, H., Kotani, M., & Yonetani, T. (1974) *Biochim. Biophys. Acta 371*, 126−139.

Ivanov, D., Sage, T. J., Markus, K., Asher, S. A., & Champion, P. M. (1994) *J. Am. Chem. Soc. 116*, 4139−4140.

Kendrew, J. C., & Parrish, R. G. (1956) *Proc. R. Soc. London, Ser. A 238*, 305−324.

Kuriyan, J., Wilz, S., Karplus, M., & Petsko, G. A. (1986) *J. Mol. Biol. 192*, 133−154.

Lambright, D. G., Balasubramanian, S., Decatur, S. M., & Boxer, S. G. (1994) *Biochemistry 33*, 5518−5525.

Lancaster, C. R. D. (1994) The coupling of light-induced electron transfer to proton uptake in the photosynthetic reaction center from Rhodopseudomonas viridis,. Ph.D. Thesis, Johann Wolfgang Goethe-University, Frankfurt am Main, Germany.

Lim, M., Jackson, T. A., & Anfinrud, P. A. (1995a) *Science 269*, 962−966.

Lim, M., Jackson, T. A., & Anfinrud, P. A. (1995b) *J. Chem. Phys. 102*, 4355−4366.

Lim, M., Jackson, T. A., & Anfinrud, P. A. (1997) *Nat. Struct. Biol. 4*, 209−214.

McRee, D. (1992) *J. Mol. Graphics 10*, 44−47.

Moffat, K. (1997) *Methods Enzymol.* (in press).

Moore, J. N., Hansen, P. A., & Hochstrasser, R. M. (1988) *Proc. Natl. Acad. Sci. U.S.A. 85*, 5062−5066.

Nienhaus, G. U., Mourant, J. R., & Frauenfelder, H. (1992) *Proc. Natl. Acad. Sci. U.S.A. 89*, 2902−2906.

Nienhaus, G. U., Mourant, J. R., Chu, K., & Frauenfelder, H. (1994) *Biochemistry 33*, 13413−13430.

Olson, J. S., & Phillips, G. N., Jr. (1996) *J. Biol. Chem. 271*, 17593−17596.

Ormos, P., Braunstein, D., Frauenfelder, H., Hong, M. K., Lin, S.-L., Sauke, T. B., & Young, R. D. (1988) *Proc. Natl. Acad. Sci. U.S.A. 85*, 8492−8496.

Otwinowski, Z. (1991) *DENZO: A Film Processing Program for Macromolecular Crystallography*, Yale University Press, New Haven, CT.

Parak, F., Hartmann, H., Aumann, K. D., Reuscher, H., Rennekamp, G., Bartunik, H., & Steigemann, W. (1987) *Eur. Biophys. J. 15*, 237−249.

Phillips, G. N., Jr. (1990) *Biophys. J. 57*, 381−383.

Phillips, S. E. V. (1980) *J. Mol. Biol. 142*, 531−554.

Phillips, S. E. V. (1981) Structure coordinates of deoxymyoglobin deposited in the Brookhaven Protein Data Bank (1MBD).

Powers, L., Chance, B., Chance, M., Campbell, B., Friedman, J., Khalid, S., Kumar, C., Naqui, A., Reddy, K. S., & Zhou, Y. (1987) *Biochemistry 26*, 4785−4796.

Quillin, M. L., Arduini, R. M., Olson, J. S., & Phillips, G. N., Jr. (1993) *J. Mol. Biol. 234*, 140−155.

Ren, Z., & Moffat, K. (1995a) *J. Appl. Crystallogr. 28*, 461−481.

Ren, Z., & Moffat, K. (1995b) *J. Appl. Crystallogr. 28*, 482−493.

Sassaroli, M., & Rousseau, D. L. (1986) *J. Biol. Chem. 261*, 16292−16294.

Schlichting, I., Berendzen, J., Phillips, G. N., Jr., & Sweet, R. M. (1994) *Nature 371*, 808−812.

Springer, B. A., Sligar, S. G., Olson, J. S., & Phillips, G. N., Jr. (1994) *Chem. Rev. 94*, 699−714.

Šrajer, V., Reinisch, L., & Champion, P. M. (1991) *Biochemistry 30*, 4886−4895.

Šrajer, V., Teng, T.-Y., Ursby, T., Pradervand, C., Ren, Z., Adachi, S., Schildkamp, W., Bourgeois, D., Wulff, M., & Moffat, K. (1996) *Science 274*, 1726−1729.

Steinbach, P. J., Ansari, A., Berendzen, J., Braunstein, D., Chu, K., Cowen, B. R., Ehrenstein, D., Frauenfelder, H., Johnson, J. B., Lamb, D. C., Luck, S., Mourant, J. R., Nienhaus, G. U., Ormos, P., Philipp, R., Xie, A., & Young, R. D. (1991) *Biochemistry 30*, 3988−4001.

Straub, J. E., & Karplus, M. (1991) *Chem. Phys. 158*, 221−248.

Takano, T. (1977a) *J. Mol. Biol. 110*, 537−568.

Takano, T. (1977b) *J. Mol. Biol. 110*, 569−584.

Teng, T.-Y., & Moffat, K. (1997) *J. Appl. Crystallogr.* (in press).

Teng, T.-Y., Šrajer, V., & Moffat, K. (1994a) *Nat. Struct. Biol. 1*, 701−705.

Teng, T.-Y., Schildkamp, W., Dolmer, P., & Moffat, K. (1994b) *J. Appl. Crystallogr. 27*, 133−139.

Vitkup, D., Petsko, G., & Karplus, M. (1997) *Nat. Struct. Biol. 4*, 202−208.

Zhu, L., Sage, J. T., & Champion, P. M. (1993) *Biochemistry 32*, 11181−11185.

BI971140X